http://eprints.gla.ac.uk/150013/

On the Numerical Modelling of Bond for the Failure Analysis of Reinforced Concrete

Peter Grassl[1,*], Morgan Johansson[2,3] and Joosef Leppänen[2]

[1] School of Engineering, University of Glasgow, Glasgow G128LT, UK

[2] Chalmers University of Technology, Göteborg, Sweden

[3] Norconsult AB, Göteborg, Sweden

[*] Corresponding author. Email: peter.grassl@glasgow.ac.uk

Abstract

The structural performance of reinforced concrete relies heavily on the bond between reinforcement and concrete. In nonlinear finite element analyses, bond is either modelled by merged, also called perfect bond, or coincident with slip, also called bond-slip, approaches. Here, the performance of these two approaches for the modelling of failure of reinforced concrete was investigated using a damage-plasticity constitutive model in LS-DYNA. Firstly, the influence of element size on the response of tension-stiffening analyses with the two modelling approaches was investigated. Then, the results of the two approaches were compared for plain and fibre reinforced tension stiffening and a drop weight impact test. It was shown that only the coincident with slip approach provided mesh insensitive results. However, both approaches were capable of reproducing the overall response of the experiments in the form of load and displacements satisfactorily for the meshes used.

Table 1: Nomenclature.

Symbol	Definition
A_c	cross-sectional area of concrete specimen
A_s	cross-sectional area of the reinforcement bar
E	Young's modulus
E_c	Young's modulus of concrete
$E_{\mathrm{k},0}$	kinetic energy before impact
E_p	plastic hardening modulus
E_s	Young's modulus of steel
F	force
F_y	yield force
f_c	compressive strength
f_ck	characteristic compressive strength
f_t	tensile strength
f_t1	stress threshold
G_F	tensile fracture energy of concrete
H_p	hardening modulus
h_e	measure of element length
h_m	average length of the two adjacent beam elements
L	Length
M_Rd	Moment capacity
m_b	effective mass of the beam
m_beam	mass of the beam
m_w	mass of the drop weight
N_s	axial force
q_h	hardening parameter
$R,\ R_\mathrm{rd}$	load capacity
W_e	external energy
W_i	internal energy
$W_\mathrm{i,el}$	elastic internal energy
$W_\mathrm{i,pl}$	plastic internal energy
s	slip
s_max	slip at which bond strength is reached
V_e	volume of element
w_c	crack opening
w_f	crack opening threshold
w_f1	crack opening threshold

Table 1: *Cont.*

Symbol	Definition
α	ratio of stiffnesses
δ	displacement
ε_c	inelastic strain
ε_f	inelastic strain threshold in compression
$\bar{\theta}$	Lode angle
κ_mF	dynamic correction coefficient
ν	Poisson's ratio
$\bar{\rho}$	length of deviatoric effective stress
ρ	density
ρ_s	ratio of areas
σ	stress
$\bar{\sigma}_\mathrm{v}$	volumetric effective stress
σ_y	yield strength
τ_b	bond stress
τ_max	bond strength
ϕ	diameter of the reinforcement bar

1 Introduction

Ductile, durable and cost effective reinforced concrete structures can be produced by designing the reinforcement arrangement and bond properties between reinforcement and matrix. The nonlinear finite element method has the potential to support the design process of reinforced concrete structures, because it is capable of producing detailed results which are difficult to extract from physical experiments. By analysing the nonlinear response of individual components, namely plain concrete, reinforcing steel and the interaction of reinforcement and concrete, detailed information about the composite response can be obtained. This requires modelling techniques, which provide a realistic description of the mechanical response of individual components. For a successful application of the nonlinear finite element method, the models need to be robust, based on input parameters which can be easily obtained and produce results independent of numerical approximation procedures, i.e. independent of mesh and step size.

For the nonlinear finite element method, one common check is to show that the results are mesh-insensitive. For plain concrete, this is a challenging task since the response in tension and low confined compression is quasi-brittle which is characterised by strain softening, i.e. decreasing stress with increasing strain. This strain softening results in localised deformation patterns in the form of cracks and shear bands. Common strategies to describe these localised deformation patterns mesh independently is to use nonlocal constitutive models [1] or to adjust the softening modulus of local constitutive models with respect to a length measure which is directly proportional to the element size. Nonlocal constitutive models are most commonly formulated as integral type nonlocal or gradient models in which the stress evaluation depends on spatial averaging of history variables [38] or spatial gradients of history variables [35], respectively. These models have shown to provide results for localised deformation patterns which are insensitive to mesh size and mesh orientation, if the mesh is chosen to be fine enough [46]. Nonlocal models are rarely used in commercial finite element programs, because they are difficult to calibrate and require very fine discretisations. Recently, a new calibration strategy for nonlocal models was proposed in [47], but more work is required to address the requirement for fine discretisation. On the other hand, crack band models based on an adjustment of the softening modulus [37, 2] are commonly used in commercial finite element programs. These models can be used with a wide range of mesh sizes and can be relatively easily calibrated. For crack band models, global results in the form of load-displacement curves are in many cases insensitive to the mesh size. However, deformation patterns are often influenced by the mesh direction, since they localise in a mesh-size dependent zone [23]. Furthermore, in general 3D analyses, there is no straightforward approach how to define the length measure which is used to adjust the softening modulus of stress-strain curves [21].

In structural analyses of reinforced concrete, reinforcement is often modelled by beam or truss elements which are connected to solid elements. The constitutive model for the reinforcement is typically based on elasto-plasticity, where the plasticity part is either hardening or perfect plastic. Therefore, for the reinforcement itself, mesh-independent modelling is not difficult. For the interaction of reinforcement and concrete, either perfect bond or bond-slip laws are

used [20]. For perfect bond, the nodes of the reinforcement are merged with those of the concrete elements, if the mesh is generated so that the location of nodes of reinforcement and concrete elements coincide. Alternatively, the degrees of freedom of the reinforcement are constrained within the concrete elements [36, 12, 20, 6]. Perfect bond is often assumed in the failure analysis of structures with good bond conditions between reinforcement and concrete, such as for the case of deformed reinforcement bars, which contain ribs to increase the load transfer between steel and concrete [7]. For poor bond conditions or more complicated loading scenarios such as cyclic loading, bond-slip laws are used, which can be included by means of nonlinear springs [32, 31, 44] or interface elements [40, 45] between coincident nodes of reinforcement and concrete elements. Alternatively, techniques to include bond-slip laws while constraining the reinforcement element within the concrete elements has been reported in [20, 43]. An investigation of constrained approaches together with damage-plasticity models has been presented in [27]. If reinforcement elements are constrained in the concrete elements, the concrete can be meshed independently from the reinforcement, which simplifies the mesh generation for complex reinforcement arrangements and hexahedral elements. Therefore, the constrained techniques are commonly used in commercial finite element programs [10, 11, 16, 20, 42, 43]. However, the numerical implementation of these constrained approaches for general conditions can be difficult.

Studies on the influence of mesh size on the response of reinforced concrete are much less frequent than for plain concrete structures. From the limited available results in the literature, it was shown that nonlocal models are able to reproduce the interaction of concrete and reinforcement mesh-independently for both perfect bond [45, 34, 46] and bond slip [45]. For crack band models, the influence of mesh dependence on crack patterns is less clear. It is generally accepted that the use of perfect bond together with crack band models produces mesh dependent crack patterns [45, 46]. In [45], it was also shown that crack patterns obtained from dynamic 2D analyses with bond-slip appear to be mesh-dependent as well.

In the present study, the modelling of reinforced concrete with perfect bond and bond-slip was further investigated by means of 3D finite element analyses using merged and coincident with slip approaches. The reinforcement was modelled by means of beam elements. The merged approach was implemented using the same nodes for the reinforcement beams and concrete. The coincident with slip approach was introduced by means of springs between coincident nodes of reinforcement and concrete as proposed in [32, 31, 44]. It was aimed to show how mesh size influences the results of 3D analysis of an elementary benchmark reproducing the tension stiffening effect of reinforced concrete. The 3D mesh size study is one of the new aspects of this study. Furthermore, it was investigated which effect the assumption of perfect bond and bond-slip has on the structural performance of reinforced concrete structures by analysing tension stiffening experiments reported in [5] and dynamic drop weight impact tests reported in [28, 26].

For concrete, the damage-plasticity constitutive model CDPM2 was used [15, 14]. In this model, plasticity is formulated in the effective stress space and damage is driven by both elastic and plastic strains. This type of combination of damage and plasticity was originally proposed by [25] and has since then been used in many constitutive models for concrete [19, 14, 9, 15]. The damage-plasticity model CDPM2 has shown to be able to reproduce important characteristics

of concrete, such as strain softening and reduction of stiffness in tension and low-confined compression, as well as increase of strength and deformation capacity in confined compression. CDPM2 has been recently implemented as material model 273 in the general purpose finite element program LS-DYNA (Release 9.1.0) [17], which was used for the present analyses.

2   Method

The influence of the way how bond is modelled on the results of three-dimensional finite element analyses of the failure of reinforced concrete structures was studied by combining models for concrete, reinforcement and the interaction of reinforcement and concrete. In the following paragraphs, the models of the different components are discussed.

For concrete, the concrete damage-plasticity model 2 (CDPM2) proposed in [15] was used, which is an extension of CDPM proposed in [14]. For the details of the model, it is referred to [14, 15]. In CDPM2, the stress evaluation is based on the damage mechanics concept of nominal and effective stresses. The nominal stress is evaluated by a combination of damage and plasticity. The effective stress in the undamaged material is determined from the plasticity part alone. For the nominal stress evaluation, tensile and compressive damage variables are applied to positive and negative components of the principal effective stress, respectively. The plasticity part of the model is formulated in the effective stress space by means of the Haigh-Westergaard stress coordinates, which are the volumetric effective stress $\bar{\sigma}_{\mathrm{v}}$, the length of the deviatoric effective stress $\bar{\rho}$ and the Lode angle $\bar{\theta}$ [22] A list of the symbols used in this work is shown in Table 1. The yield surface is based on an extension of the failure envelope in [29]. This failure envelope is characterised by curved meridians and deviatoric sections varying from almost triangular in tension to almost circular in highly confined compression (Figure 1).

During hardening in the pre-peak regime, the yield surface is capped both in hydrostatic tension and compression. At peak, the failure surface proposed in [29] is reached, which is open in hydrostatic compression. In the post-peak regime, the yield surface undergoes further hardening, controlled by the hardening modulus H_{p}, which is designed to be greater than zero. The greater the value of H_{p}, the smaller is the contribution of plasticity in the post-peak regime. Even for H_{p} almost equal to zero, the softening response will still be a combination of damage and plasticity, since the plasticity part will produce an almost perfect plastic response, but not softening. The terms pre- and post-peak refer to the response in the nominal stress space for the case that no strain rate effects are considered. For this case, the pre-peak regime is modelled by the plasticity approach only.

The post-peak response is the result of a combination of plasticity and damage. Evolution laws for tensile and compressive damage variables are formulated as functions of the positive and negative parts of the principal effective stress. The resulting damage formulation is orthotropic. With these two damage variables, the tensile and compressive softening response can be described independently of each other.
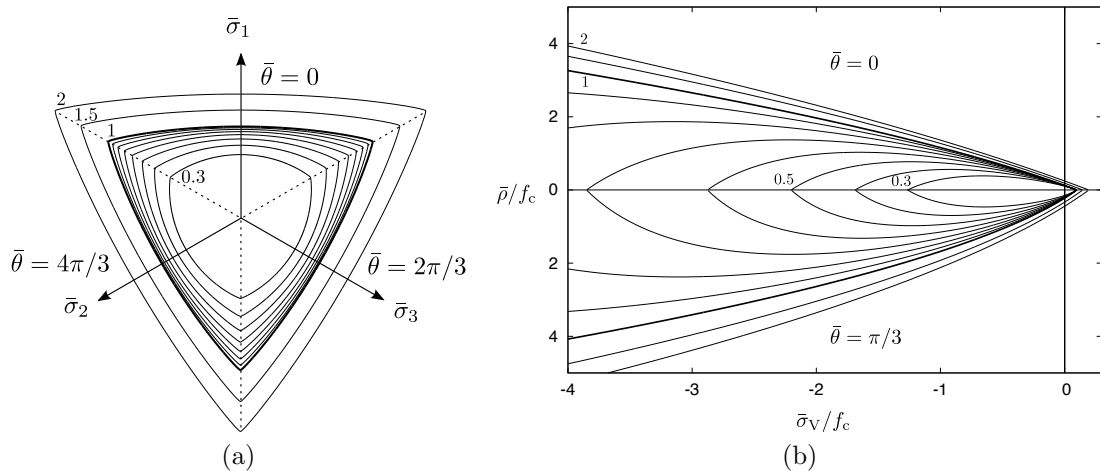
Figure 1: Evolution of the yield surface for varying hardening parameters q_h (from 0.3 to 2) which is smaller than 1 in the pre-peak and larger than 1 in the post-peak regime: (a) Deviatoric section for a constant volumetric stress of $\bar{\sigma}_v = -f_c/3$ (b) meridians at $\theta = \pi/3$ (compression) and $\theta = 0$ (tension). The failure surface at which $q_h = 1$ is indicated by a thicker line.

For tensile loading, deformation patterns are commonly mesh-dependent if local softening stress-strain laws are used, which are independent of the mesh size. Therefore, the tensile damage variable is linked to a bilinear stress-crack opening (σ-w_c) curve shown in Figure 2a. The tensile fracture energy of concrete G_F is defined as the area under the stress-crack opening curve. For the present bilinear curve, this results in $G_F = (f_t w_{f1} + f_{t1} w_f)/2$. For the default in CDPM2, $f_{t1} = 0.3 f_t$ and $w_{f1} = 0.15 w_f$, so that $G_F = 0.225 f_t w_f$. Thus, the crack opening threshold is related to the area under the stress crack opening curve (fracture energy) as $w_f = 4.444 G_F/f_t$. This value cannot be directly used as input for the finite analysis with LS-DYNA, since for the crack band approach in LS-DYNA, the inelastic strain is determined as $\varepsilon_c = w_c/h_e$, where h_e is a measure of the element length determined as a function of the volume of the element as $h_e = \sqrt[3]{V_e}$. For direct tension tests using tetrahedral elements, this approach of estimating the element length results in an overestimation of the fracture energy obtained in simulations [21]. In [13], it was shown that for tetrahedral meshes used in a three-point bending analysis, this overestimation can be corrected by multiplying the value of w_f by a factor of 0.56. Thus, in this study, the expression for determining the crack threshold was $w_f = 0.56 \times 4.444 G_F$.

The compressive damage variable is linked to a stress-inelastic strain curve (Figure 2b), since the deformation patterns in the compressive zones of bending dominated applications are often mesh-size independent [15].

CDPM2 requires many input parameters, which can be divided into groups related to the elastic, plastic and damage parts of the model. In the present work, most of these parameters are set to their default values provided in [15], where it was shown that they provide a good match with experimental results. Some of the parameters which are directly linked to experimental results, such as density ρ, Young's modulus E, Poisson's ratio ν, tensile strength f_t, compressive strength f_c, fracture energy G_F, and damage threshold w_f were adjusted to match material data available
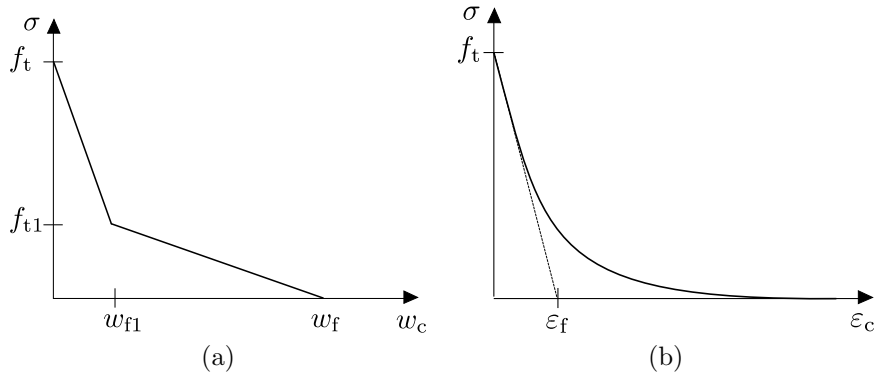
Figure 2: Softening responses used to determine damage variables: (a) Bilinear stress-crack opening curve used to determine tensile damage variable, (b) Exponential stress-inelastic strain curve used for the evaluation of the compressive damage variable.

for the different groups of analyses. Furthermore, the default value for the inelastic strain threshold ε_f (Figure 2) results in a very brittle response in compression. Therefore, it is sometimes required to choose a more ductile compressive response to avoid premature failure in regions close to supports or applied loads by choosing a greater value for ε_f than the default. This was done in the present study for the drop weight impact test in section 4.2.

The response of the steel reinforcement was modelled by beam elements with an elasto-plastic constitutive law with linear hardening. The input parameters of the constitutive law are density ρ, Young's modulus E, yield strength σ_y and plastic hardening modulus E_p.

The interaction between reinforcement and concrete was modelled by two approaches, called merged and coincident with slip. For the merged approach, the nodes of the beam and solid elements are the same. Commonly, this approach is called perfect bond, since slip between concrete and reinforcement is prevented. However, the term perfect bond is slightly misleading, since, if fine meshes are used, slip also occurs due to shear deformations in solid elements adjacent to the beam elements. For all analyses in this study, irregular tetrahedral meshes were used, which were generated with the mesh generator T3D [41]. For these type of elements, the merged approach allows for the generation of irregular meshes with the additional constraint that nodes of beam and solid elements are the same.

For the coincident with slip approach the geometry of the mesh was generated in the same way as for the merged approach. However, the nodes which connect beam and solid elements are duplicated, so that for these connecting locations, sets of coincident nodes are obtained. The interaction of the beam and solid elements is then modelled by three orthogonally orientated springs which are inserted between the coincident nodes [31]. One spring is aligned with the average axial direction of the two adjacent beam elements. This spring represents the bond-slip law between reinforcement and concrete. For the other two springs in lateral directions to the average beam axis, elastic spring stiffnesses are used, which are chosen to be large enough to avoid excessive relative movement, but small enough to avoid numerical complications. For the axial spring, the nonlinear relation of force F and displacement s is chosen as
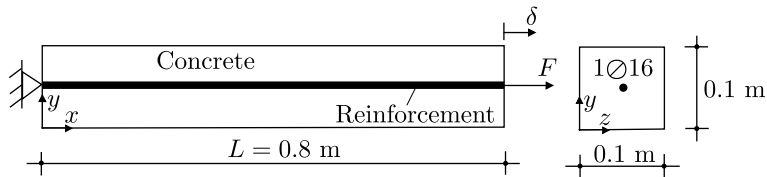
Figure 3: Mesh sensitivity study: Geometry and loading setup.

$$F = \tau_{\mathrm{b}}(s)\pi\phi h_{\mathrm{m}} \tag{1}$$

Here, the displacement s is the slip, i.e. relative displacement, between the reinforcement and the concrete, ϕ is the diameter of the reinforcement and h_{m} is the average length of the two adjacent beam elements. In the analyses in this work, the beams representing reinforcement were straight and meshed regularly. Consequently, the length h_{m} was equal to the length of the beam elements.

The function $\tau_{\mathrm{b}}(s)$ describes the bond-slip law, which in the present study is chosen as

$$\tau_{\mathrm{b}} = \begin{cases} \tau_{\max}\left(\dfrac{s}{s_{\max}}\right)^{0.4} & \text{if } s < s_{\max} \\ \tau_{\max} & \text{if } s \geq s_{\max} \end{cases} \tag{2}$$

where $\tau_{\max}$ is the bond strength and $s_{\max}$ is the slip at which the bond strength is reached. The first part of (2) for $s < s_{\max}$ is identical to the CEB-FIP Model Code [8] for ribbed bars with good bond conditions. The second part was chosen here to be constant, as done previously in [40, 45], whereas in the CEB-FIP Model Code a softening relation is used. For the present analyses in which the reinforcement yields before the anchorage capacity has been reached, the slip encountered was less than $s_{\max}$. Therefore, the second part of the bond law in (2) is considered of no importance for the present study. According to the CEB-FIP Model Code [8], the bond strength was $\tau_{\max} = 2\sqrt{f_{\mathrm{ck}}}$. Here, the characteristic compressive strength f_{ck} was obtained by subtracting 8 MPa from the mean compressive strength [8].

3   Mesh sensitivity study

In the first study, it was investigated if the two approaches for modelling the interaction of reinforcement and concrete produce mesh insensitive results in combination with a crack-band approach for concrete. The geometry and loading setup of the numerical test is shown in Figure 3. It consists of a concrete prism of length $L = 0.8$ m with a cross-section of 0.1×0.1 m^2 containing a single reinforcement bar of a diameter of 16 mm. The load was applied in the form of a monotonically increasing displacement δ at the right end of the reinforcement bar. The other end of the reinforcement bar was fixed. The concrete was not supported. Explicit dynamic analyses using the Finite Element
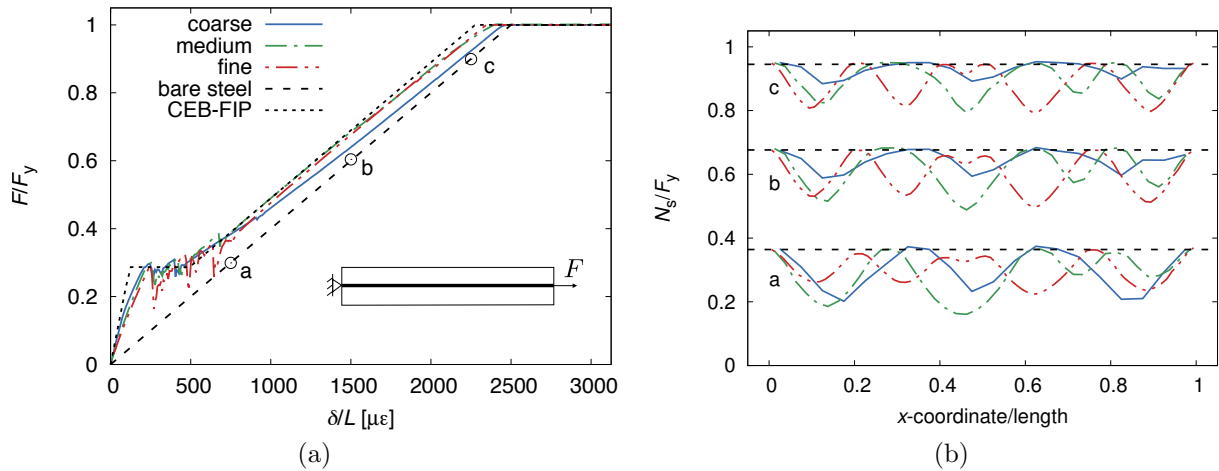
Figure 4: Mesh sensitivity study: Influence of three meshes sizes for the merged approach on (a) normalised load versus strain and (b) normalised axial force of the steel bar along the specimen length for three load levels marked in part (a) of the figure.

Program LS-DYNA (Release 9.1.0) [17] with a constant prescribed end displacement rate of 3 mm/s were used to simulate quasi-static loading. The total duration of the loading was 1 s. It was checked that decreasing the loading rate further changed the results only insignificantly.

The input parameters were chosen to be typical for reinforced concrete but were not based on any experimental results, since this part of the study was limited to a mesh sensitivity study. For concrete, the input parameters for the damage-plasticity model CDPM2 were $\rho = 2300$ kg/m^3, $E = 20$ GPa, $\nu = 0.2$, $f_t = 2.4$ MPa, $f_c = 24$ MPa, $G_F = 100$ N/m. The strain rate effect on the material properties was not considered and the hardening modulus was set to $H_p = 0.01$. The value of the fracture energy G_F corresponds to a displacement threshold of $w_f = 0.56 \times 4.444 \times G_F/f_t = 103.7 \times 10^{-6}$ m for the bilinear law described in Section 2. All other input parameters were chosen according to their default values in [15]. For the reinforcement, the input parameters were $\rho = 7850$ kg/m^3, $E = 200$ GPa, $\nu = 0.3$, yield stress $\sigma_y = 500$ MPa and plastic hardening modulus $E_p = 0$. For the coincident with slip approach, the additional parameters of the bond-slip law were $s_{max} = 0.6$ mm and $\tau_{max} = 8$ MPa according to [8]. Three tetrahedral meshes with approximate element edge lengths h_e of 40, 20 and 10 mm were generated using T3D [41], so that nodes of beam and tetrahedral elements coincide. Only for the beam elements representing the reinforcement, the used element lengths were exact, since the beams were discretised regularly.

The results are presented in the form of normalised load versus strain, normalised axial force diagram of the steel bar and contour plots of the maximum principal strains in the concrete specimen. The first set of results is for the merged approach. The normalised load versus strain curves for the three meshes are shown in Figure 4a together with the response of the bare steel. The normalised axial force N_s of the steel versus the normalised x-coordinate at three load levels marked in Figure 4a are shown in Figure 4b. The force is normalised by the yield force $F_y = A_s\sigma_y$, where A_s is the cross-sectional area of the reinforcement bar. The second set of results are for the coincident with
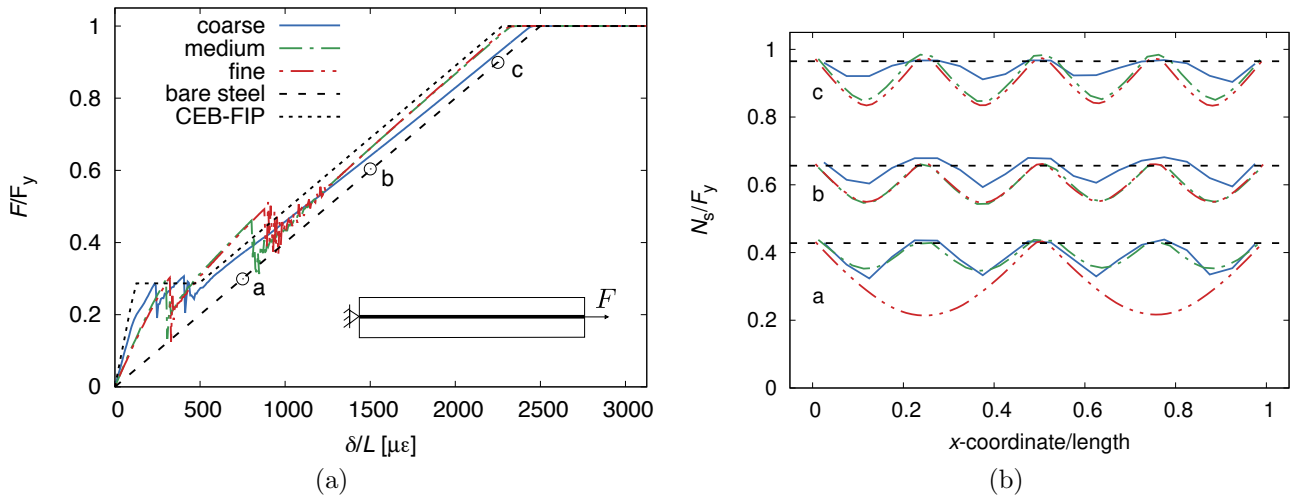
10

Figure 5: Mesh sensitivity study: Influence of three mesh sizes for coincident with slip approach on (a) normalised load versus strain and (b) normalised axial force of the steel bar along the specimen length for three load levels marked in part (a) of the figure.

slip approach. The normalised load-strain curves are shown in Figure 5a. The normalised axial force of the steel bar versus the normalised x-coordinate at three load levels marked in Figure 5a are shown in Figure 5b.

For both approaches, the contour plots of the maximum principal strain are shown in Figure 6. Here, the colour black refers to maximum principal strain equal or greater than 0.04 mm/h_e. This threshold was chosen to be mesh-dependent so that for all meshes, the colour black refers to the same crack opening, since the elastic strain component is much smaller than the inelastic strain component. The main cracking phase occurs between 30 and 50 % of the yield load. In all analyses, tension stiffening is visible in the form of difference in the displacement of the reinforced concrete prism and the plain steel bar at the same load level (Figures 4a and 5a). This difference is caused by the stress transfer from the steel into the concrete faciliated by the bond between the two materials. In section in which the both the steel and concrete contribute to the force transfer, the force in the steel is less than in sections in which only the steel transfer the force. This reduction of the steel force due to the action of the concrete results in a smaller displacement of the steel bar. The tension stiffening reproduced by the coarse mesh is less than for the fine mesh. At yielding, the axial force is almost equal to the yield force, because the stress in the damaged region is close to zero. However, the normalised axial diagrams for the two approaches in Figures 4b and 5b reveal significant differences. For the merged approach in Figure 4b, the positions of peaks of axial force in the reinforcement, which corresponds to the location of cracks, is dependent on the mesh size. Furthermore, the number of cracks is mesh dependent as well. This dependence of crack position and number on mesh size for the merged approach is also visible in the contour plots (Figure 6). On the other hand, the coincident with slip approach provides mesh-independent results (Figure 5b). Both the position of the cracks as well as the number of cracks is independent of the mesh size. The agreement of the analyses with different element sizes is particularly good for the medium and fine mesh. Despite this dependence on mesh size for the merged approach, both approaches produce mesh-independent normalised force-strain curves for the
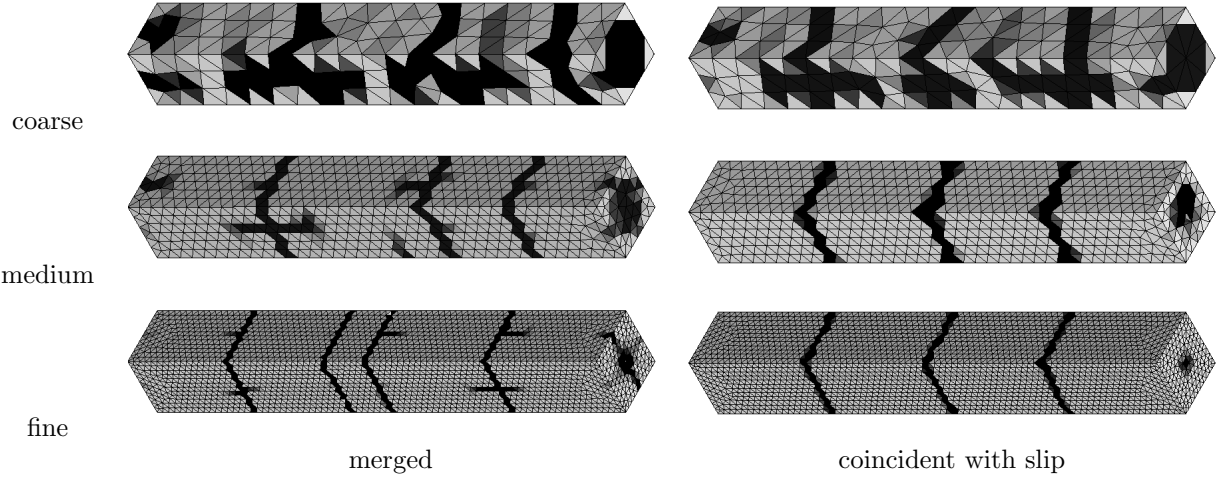
Figure 6: Mesh sensitivity study: Contour plot of maximum principal strain for coarse, medium and fine meshes for merged and coincident with slip approaches. Black and light grey correspond to large and small maximum principal strains, respectively.

medium and the fine mesh. This is because the integral of the reduction of the axial force along reinforcement with respect to the applied load level in Figure 4b is similar, although the position and number of axial force reductions differs. Comparing the green and red lines in Figure 4b shows that between the two cracks (high values of axial force) in the middle of the fine mesh, the steel force does not reduce significantly. Thus, the additional crack generated in the fine mesh compared to the medium one does not influence the amount of tension stiffening significantly.

The results show that the crack approach together with the coincident with slip approach provides mesh-independent crack patterns for reinforced concrete structures, if the mesh size is small enough. These 3D findings complement the 2D results obtained in [46], where it was shown that crack band and merged approaches together provide mesh-dependent results, but nonlocal models with the merged approach show a mesh insensitive response.

In Figures 4 and 5, the numerical results are compared with an analytical approximation of the tension stiffening response of such a prism, which was proposed in the CEB-FIP textbook on updated knowledge of the CEB/FIP Model Code [30]. For this approximation, the response is divided into four stages:

$$
F = \begin{cases}
E_\mathrm{c} A_\mathrm{c} \left(1 + \alpha \rho_\mathrm{s}\right) \dfrac{\delta}{L} & \text{for } 0 < \delta/L \le f_\mathrm{t}/E_\mathrm{c} \\[2ex]
A_\mathrm{c} f_\mathrm{t} \left(1 + \alpha \rho_\mathrm{s}\right) & \text{for } f_\mathrm{t}/E_\mathrm{c} < \delta/L \le f_\mathrm{t} \dfrac{0.6 + \alpha \rho_\mathrm{s}}{E_\mathrm{s} \rho_\mathrm{s}} \\[2ex]
A_\mathrm{s} E_\mathrm{s} \left(\delta/L + \dfrac{0.375 f_\mathrm{t}}{E_\mathrm{s} \rho_\mathrm{s}}\right) & \text{for } f_\mathrm{t} \dfrac{0.6 + \alpha \rho_\mathrm{s}}{E_\mathrm{s} \rho_\mathrm{s}} < \delta/L < \sigma_\mathrm{y}/E_\mathrm{s} - \dfrac{0.375 f_\mathrm{t}}{E_\mathrm{s} \rho_\mathrm{s}} \\[2ex]
F_\mathrm{y} & \text{for } \sigma_\mathrm{y}/E_\mathrm{s} - \dfrac{0.375 f_\mathrm{t}}{E_\mathrm{s} \rho_\mathrm{s}} < \delta/L
\end{cases}
\tag{3}
$$

In (3), E_c and A_c are the Young's modulus and cross-sectional area of concrete, respectively. Furthermore, $\alpha = E_\mathrm{s}/E_\mathrm{c}$ and $\rho_\mathrm{s} = A_\mathrm{s}/A_\mathrm{c}$. In the first part of (3), concrete is assumed to be uncracked and the strain in the concrete and steel are
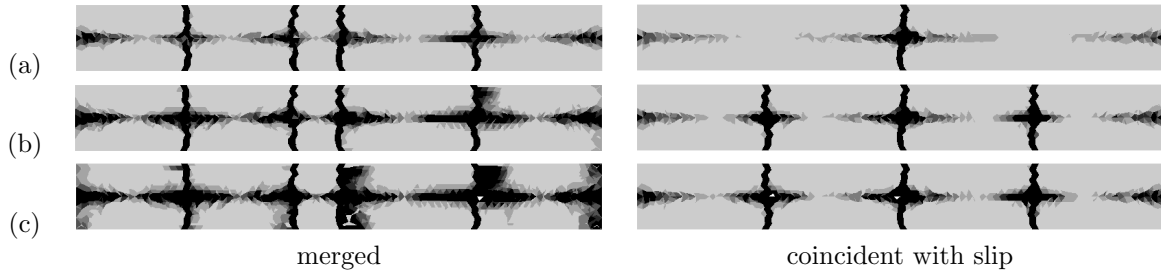
Figure 7: Mesh sensitivity study: Contour plot of maximum principal strain for the fine meshes for merged and coincident with slip approaches in the x-z section at $y = 0.05$ m at three load levels marked in Figures 4 and 5. Black and light grey correspond to large and small maximum principal strains, respectively.

assumed to be equal throughout the length of the specimen. This does not reproduce the situation in the numerical analyses, since in the analysis the force is only applied to the ends of the reinforcement bar and not the concrete faces, so that slip between the concrete and the reinforcement occurs at the end of the specimens. Consequently, the numercial response is softer than the one predicted by the analytical solution. In (3), the uncracked stage is followed by a crack formation phase during which the load is assumed to be constant. This is an idealisation of the response observed in experiments in which the crack formation phase is accompanied by an increase of the normalised load. For the numerical analyses, the merge approach predicts only a small increase of the normalised load during the cracking stage, with the majority of the cracking occurring at approximately 30 % of the yield load, which is in very good agreement with the analytical solution. However, for the coincident with slip approach, the cracking phase occurs at two distinct stages at around 30 and 45 % of the yield load. In the next stage in (3), cracking is stabilised and the response of the reinforced specimen is parallel to the one of the bare steel bar. Finally, the yielding of the reinforcement occurs. Overall, the analytical approximation is in good agreement with the numerical results. Particularly, the normalised load versus strain curves for the merged approach for the medium and fine mesh are in very good agreement with this simplified approach.

A more detailed comparison of the contour plots for the merged and coincident with slip approaches reveals differences in the crack evolution. For the merged approach, the contour plots of the maximum principal strain show longitudinal surface cracks along the reinforcement bar which are not visible for coincident with slip approach. To investigate the crack evolution further, contour plots of the maximum principal strain are compared for the two approaches in the x-z plane at $y = 0.05$ m in Figure 7 at the three load levels marked in Figures 4 and 5. For both approaches, significant cracking occurs in the centre of the specimen along the position of the reinforcement bar. This cracking is slightly more prominent for the the merged approach than the coincident with slip approach, but is also clearly visible for the latter. For the merged approach, the perpendicular cracks have all formed already at load level a, which is in agreement with the results in Figure 4. For the coincident with slip approach, the first perpendicular crack in the middle of the specimen formed at load level a. Then, at load level b all three perpendicular cracks have formed. The detailed contour plots highlight that the merged approach does not correspond to a "perfect bond" situation. Although the nodes of reinforcement and concrete have the same degrees of freedom in the axial direction, there

13

is relative displacement between the concrete prism and the reinforcement due to the cracking in the longitudinal direction along the reinforcement bar. This is the reason why the merged approach results in a limited number of perpendicular cracks. The amount of slip will depend on the type of constitutive model used for the concrete. In the present study, the constitutive model is capable of reproducing the general concrete response from multi-axial tension to high confined compression.

If the benchmark was modelled by a single row of elements, the merged approach would produce cracks in every element along the reinforcement bar, once the stress in the concrete reaches the strength. Thus, the finer the mesh, the more elements crack. This would produce mesh-dependent results. The reason why the present 3D analyses do not show cracking in every element is because the mesh is relatively fine. As a result, there are deformations in the elements adjacent to the reinforcement bar, which act in a way similar as a bond-slip model. However, these deformations are mesh-dependent, which results in the observed mesh-dependent results. For the coincident with slip approach, the relative displacement between steel and concrete is dominated by the introduced bond-slip model, which is based on a mesh-independent force-displacement law. Therefore, the results are mesh-independent using this approach. However, since the longitudinal cracking is also visible for the coincident with slip approach, it influences the relative displacement between the interaction of reinforcement and concrete. If it is assumed that bond-slip laws are commonly extracted from experiments in which the slip is the relative displacement between concrete and reinforcement, the bond-slip law used in analyses should be ideally determined from an inverse analysis.

4   Comparison with experiments

The merged and coincident with slip approaches were applied to the analysis of two experiments reported in the literature. In the previous section, it was shown that the two approaches provide almost mesh independent load-displacement curves for tension stiffening analyses, but that the crack patterns obtained with these approaches differ. The merged approach provides mesh-dependent crack patterns, whereas the crack patterns obtained with the coincident with slip approach is mesh-independent. In the following two sections the performance of the two approaches will be further investigated by comparing them with experimental results.

4.1   Tension stiffening experiments

In the first set of analyses, tension stiffening experiments for plain and fibre reinforced concrete reported in [5] were simulated. This type of experiment is commonly used to determine the mean crack spacing of reinforced concrete [4, 5]. In the experiments in [5], it was shown that the use of fibre reinforced concrete results in smaller crack spacing than for plain concrete. Here, it is investigated if the merged and coincident with slip approach are capable to reproduce the influence of the type of concrete on the crack spacing. The geometry and loading setup is shown in Figure 8,
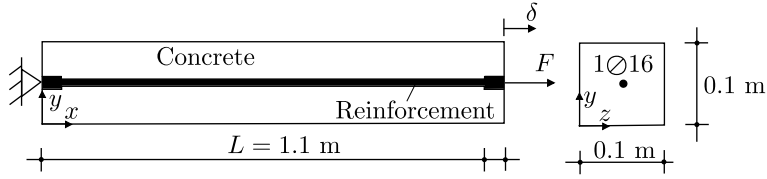
Figure 8: Tension stiffening experiment: Geometry and loading setup according to [5].

which is longer than the specimen in section 3, but otherwise of very similar geometry. Again, it consists of a concrete prism with a single reinforcement bar centrically embedded. Both load, in the form of a prescribed displacement, and, support are applied to the ends of the reinforcement directly. One difference is that, the 40 mm end regions of the reinforcement were made of a larger diameter ($\phi = 19.5$ mm) so that bridging stresses across cracks present in the fibre reinforced concrete did not result in yielding at the end of the reinforcement bar before yielding in a cracked section would occur [5].

The input parameters were chosen to match as much as possible the experimental results. For plain concrete, the input parameters for the damage-plasticity model CDPM2 were $\rho = 2300$ kg/m^3, $E = 39.7$ GPa, $\nu = 0.2$, $f_\mathrm{t} = 5.42$ MPa, $f_\mathrm{c} = 62.8$ MPa, $G_\mathrm{F} = 153$ N/m. The strain rate effect on the material properties were not considered and the hardening modulus was set to $H_\mathrm{p} = 0.01$. The value of the fracture energy G_F resulted in a displacement threshold of $w_\mathrm{f} = 0.56 \times 4.444 \times G_\mathrm{F}/f_\mathrm{t} = 70.1 \times 10^{-6}$ m. All other input parameters were chosen according to their default values in [15]. For fibre reinforced concrete, a modified bi-linear stress-crack opening curve was used to simulate the effect of the presence of fibres. The first displacement threshold in Figure 2a was set to $w_\mathrm{f1} = 0.15 w_\mathrm{f} = 0.15 \times 70.1 \times 10^{-6} = 10.5 \times 10^{-6}$ m, as it was done for plain concrete according to the recommended input for CDPM2. Also, the intermediate stress value was set to its default value $f_\mathrm{t1} = 0.3 f_\mathrm{t}$. The final threshold was set to $w_\mathrm{f} \to \infty$, i.e. the inclination of the second branch of the stress-crack opening curve was set to zero. All other parameters where kept the same as for plain concrete. Thus, it was assumed that the initial fracture energy of plain and fibre reinforced concrete is the same, but the bridging stress across the crack remains constant at f_t1 for fibre reinforced concrete. Shrinkage measured in the experiments in [5] has been considered in the numerical analyses in LS-DYNA using the techniques described in [43]. With this technique, the explicit dynamic simulation was preceded by an implicit stage at which a shrinkage strain of $\varepsilon_\mathrm{s} = 470 \times 10^{-6}$, as reported in [5], was applied. For the reinforcement, the input parameters were $\rho = 7850$ kg/m^3, $E = 202$ GPa, $\nu = 0.3$, $\sigma_\mathrm{y} = 420$ MPa and $E_\mathrm{p} = 0$. For the coincident slip approach, the parameters of the bond-slip law were $s_\mathrm{max} = 0.6$ mm and $\tau_\mathrm{max} = 14.8$ MPa according to the CEB-FIP Model Code 1990 [8]. A tetrahedral mesh with an approximate element edge length of $h_\mathrm{e} = 10$ mm was used.

For plain concrete, the response of the nonlinear finite element model with the merged and coincident with slip approach are presented in Figure 9 in the form of normalised load versus average strain and normalised axial force in the reinforcement at three load levels marked in the load-strain curve. The strain is calculated as $\varepsilon = \delta/L$, where δ is the end displacement of the reinforcement and L is the length of the specimen. The normalised load-strain plots in
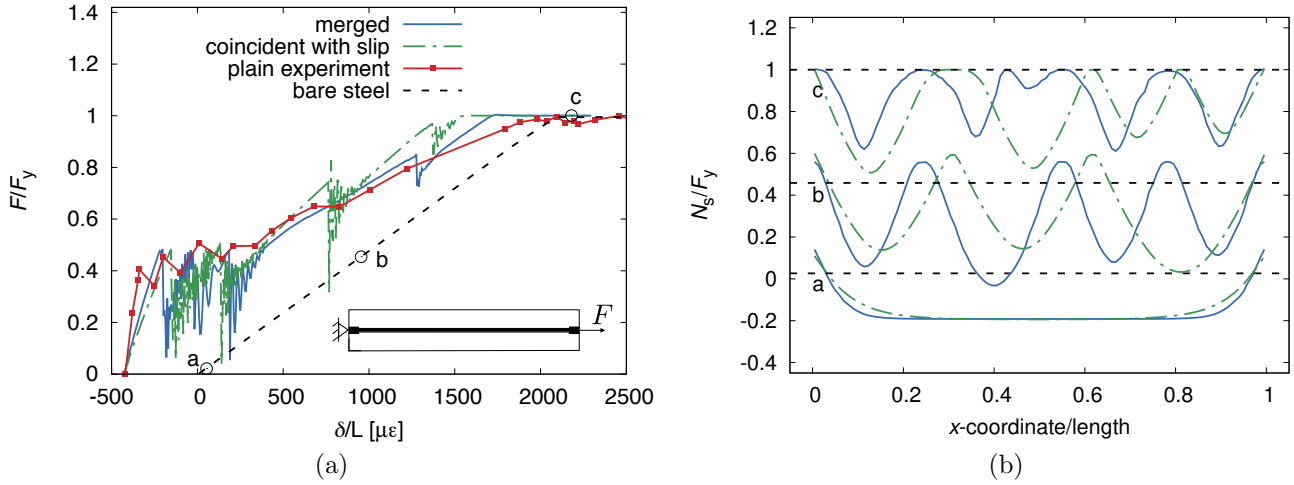
Figure 9: Tension stiffening experiment for plain concrete: Comparison of finite element results with merged and coincident with slip approach compared to experiments reported in [5] in the form of (a) normalised load versus average strain and (b) normalised axial force in the reinforcement at three load levels marked in the load-strain curve.

Figure 9a are overall in good agreement with the experiments and the tension stiffening effect is well represented by both the merged and coincident with slip approach. The normalised axial force distribution in Figure 9b shows that similar to the results for the mesh sensitivity study the merged approach produces more cracks, indicated by the peaks in axial force, than the coincident with slip approach. Both approaches underestimate the number of cracks observed in the experiments. In the simulations for plain concrete, the average crack spacing was 220 mm for the merged approach and 275 mm for the coincident with slip approach, whereas in the experiments an average crack spacing of 152 mm was reported [5]. For load level a, the normalised axial force is for both approaches in compression along the majority of the specimen, because of the initially applied shrinkage strain. For fibre reinforced concrete, the results are presented in Figure 10. Again, the normalised load versus average strain curves of the analyses match well the experimental results, despite the use of the highly idealised stress-crack opening curve. At yielding of the reinforcement, the axial force transmitted at the ends of the reinforcement bar is greater than the yield force of the reinforcement, because of the bridging stress provided by the fibres that is transmitted across the cracks (Figure 10a). In comparison, for plain concrete, the cracks were almost stress free at this stage so that axial force and yield force coincided at the onset of yielding (Figure 9a). This additional stress transfer across the cracks is also visible in Figure 10b, where it is shown that the axial force at the end of the reinforcement bar is higher than within the specimen. The average crack spacings of the merged and coincident with slip approaches are 138 mm and 183 mm, respectively, whereas the experimental crack patterns show a spacing of 85 mm. Again, the numerical simulations overestimate the crack spacing. However, the simulations predicted the reduction of crack spacing due to the presence of fibres, which was represented by a change of the stress-crack opening curve. The numerically obtained crack patterns are also shown in the form of contour plots of the maximum principal strain for plain and fibre reinforced concrete in Figure 11. Here, black corresponds to a maximum principal strain which is equal or greater than 0.008.
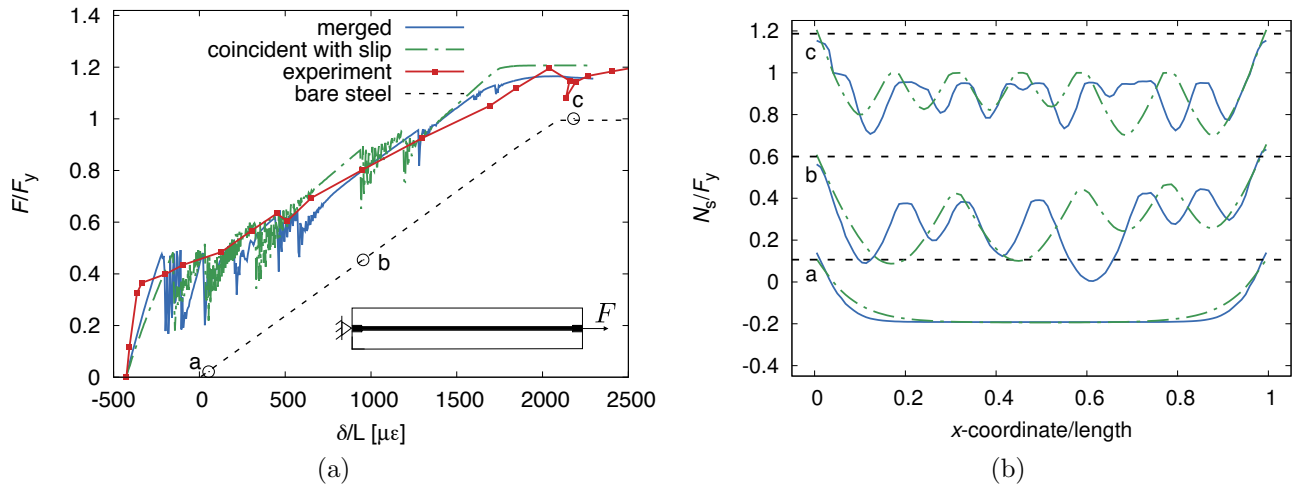
16

Figure 10: Tension stiffening experiment for fibre reinforced concrete: Comparison of finite element results with merged and coincident with slip approach compared to experiments reported in [5] in the form of (a) load versus average strain and (b) normalised axial stress in the reinforcement.
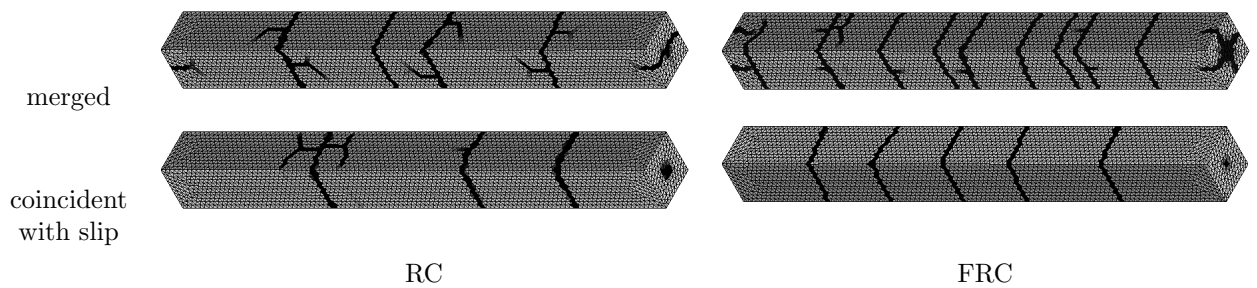

Figure 11: Tension stiffening experiment: Contour plot of maximum principal strain for merged and coincident with slip approaches for plain and fibre reinforced concrete. Black and light grey correspond to large and small maximum principal strains, respectively.
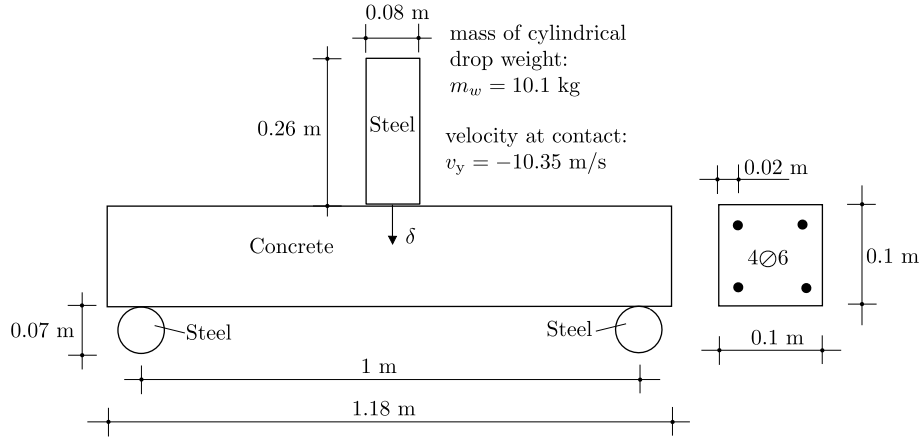
Figure 12: Drop weight impact test: Geometry and loading setup of a drop weight impact test for a reinforced concrete beam in [28, 26].

4.2 Drop weight impact test

The second set of analyses were aimed to reproduce experimental results of drop weight impact tests reported in [28, 26]. In these experiments, a cylindrical steel weight with mass 10.1 kg was dropped from a height of 5.5 m onto a simply supported concrete beam reinforced with four symmetrically arranged steel bars. The geometry and setup of the drop weight impact test is shown in Figure 12. The input parameters were chosen based on the experimental results reported in [28, 26]. For concrete, the input parameters for the damage-plasticity model CDPM2 were $\rho = 2400$ kg/m^3, $E = 34.7$ GPa, $\nu = 0.2$, $f_t = 3.28$ MPa, $f_c = 45.5$ MPa, $G_F = 113$ N/m. The strain rate effect on the response of concrete was not considered and the hardening modulus of the plasticity part was set to $H_p = 0.01$. The value of the fracture energy G_F resulted in a displacement threshold of $w_f = 0.56 \times 4.444 \times G_F/f_t = 86 \times 10^{-6}$ m. The strain threshold from the inelastic stress-strain curve in Figure 2b for the determination of the compressive damage variable was increased from the default value from 1×10^{-4} to $\varepsilon_f = 1 \times 10^{-3}$ to avoid premature failure of the region below the point at which the drop weight impacts the concrete specimen. All other input parameters were chosen according to their default values [15]. The drop weight was modelled to be elastic with the input parameters $\rho = 7753$ kg/m^3, $E = 200$ GPa and $\nu = 0.3$. In the experiments, the drop weight contained a hole, which was not modelled here. Instead, the density was adjusted so that the correct weight was obtained. Furthermore, the drop weight in the experiments had a curved head with a radius of 400 mm [28, 26], which was not considered in the analysis. For the reinforcement, the input parameters were $\rho = 7850$ kg/m^3, $E = 200$ GPa, $\nu = 0.3$, $\sigma_y = 610$ MPa and $E_p = 584$ MPa. For the coincident slip approach, the parameters of the bond-slip law were $s_{max} = 0.6$ mm and $\tau_{max} = 12.2$ MPa according to the CEB-FIP Model Code 1990 [8]. A tetrahedral mesh with an approximate element edge length of 5 mm was used. The mesh is finer than in the previous set of analyses, since in the drop weight impact tests a reinforcement diameter of 6 mm was used, instead of the 16 mm one in the tension stiffening experiment [5]. Therefore, the crack spacing in the drop weight impact test is expected to be much smaller than in the tension stiffening experiment in sections 3 and 4.1, since it is known that crack spacing decreases with decreasing diameter of the reinforcement bar
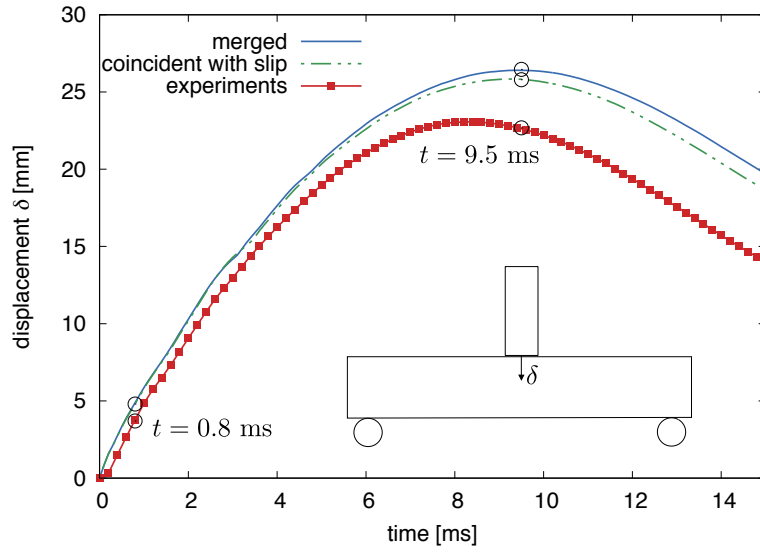
Figure 13: Drop weight impact test: Comparison of displacement δ of the top middle of the beam versus time for numerical analyses with merged, coincident with slip and experimental results reported in [28, 26].

[8].

In Figure 13, the results with the merged and the coincident with slip approach are presented in the form of the displacement δ versus time for the middle top of the beam at the point where the weight impacts the beam (Figure 12). The mean of five experimental displacement versus time curves is shown in comparison to the numerical results. The numerical maximum principal strain contour plots representing crack patterns for the two approaches are compared to Digital Image Correlation (DIC) results for one of the experiments in Figures 14 and 15 for two stages at 0.8 and 9.5 ms, respectively, marked in Figure 13. DIC has been used in the past to record cracking processes in reinforced concrete structures [18, 33] and has been shown to work for high speed processes [39]. In the present experimental study, a high speed camera was used to take images every 2 ms. The software GOM-correlate was then used to apply DIC to the images taken from the high speed camera. For the contour plots obtained from the simulations, black corresponds to a maximum principal strain equal or greater than 0.016. For the experimental DIC, black corresponds to crack openings which would correspond to stress free cracks. However, the exact value of the crack opening was not determined from the experiments. The displacement versus time curves for the two approaches are overall in good agreement with the experimental results. Furthermore, the strain contours of both approaches represent well the crack patterns observed in the experiments. Closer inspection reveals differences in the results of the two approaches. The use of the merged approach results in more cracks than the one of the coincident with slip approach. This is in agreement with the results presented in the previous sections in which the crack spacing obtained with the merged approach is smaller than with the coincident with slip approach.

As a comparison with the experimental and numerical results of the drop weight test, a rough estimate of the expected mid-beam displacement is made using a simplified calculation. This estimate is based on energy equilibrium, theory
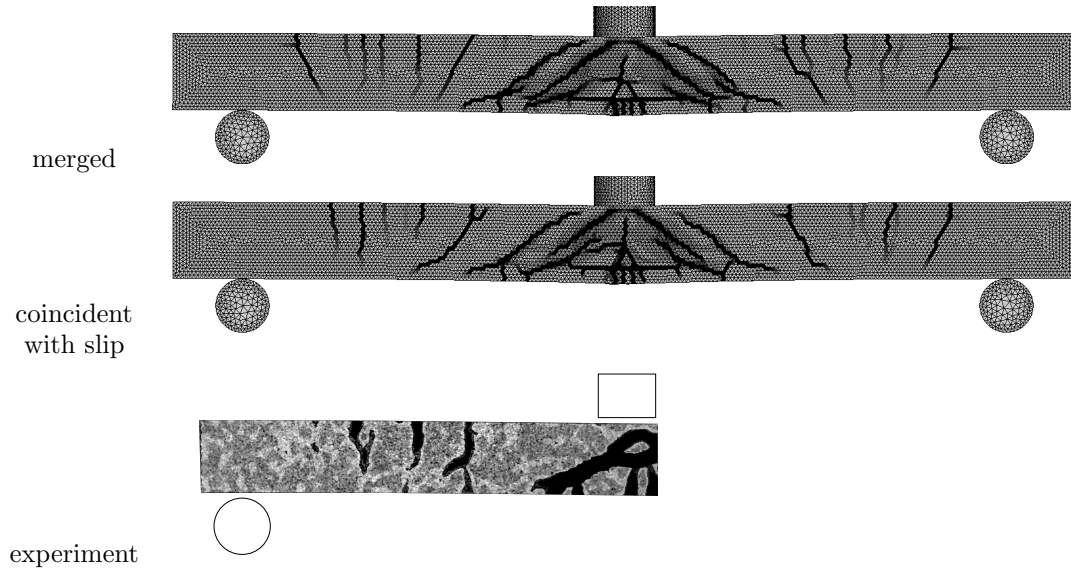
19

Figure 14: Drop weight impact test: Contour plot of maximum principal strain for merged and coincident with slip approaches compared to DIC results from experiments reported in [28, 26] at 0.8 ms. For the finite element analyses, black and light grey correspond to large and small maximum principal strains, respectively. For the experimental DIC results, black refers to large crack opening.
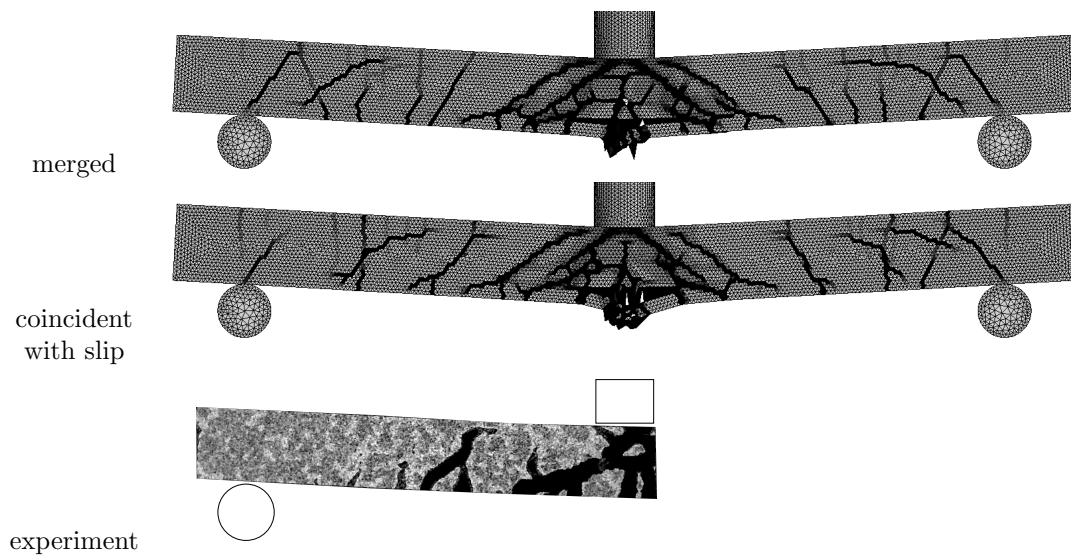

Figure 15: Drop weight impact test: Contour plot of maximum principal strain for merged and coincident with slip approaches compared to DIC results from experiments reported in [28, 26] at 9.5 ms. For the finite element analyses, black and light grey correspond to large and small maximum principal strains, respectively. For the experimental DIC results, black refers to large crack opening.
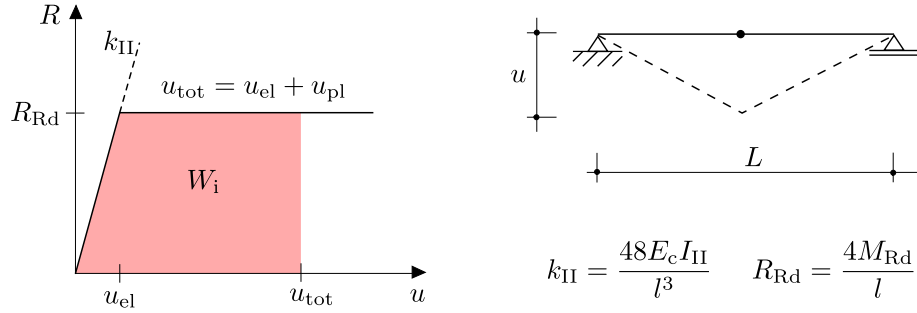
Figure 16: Drop weight impact test: Simplified bilinear load-displacement relation used for the reinforced beam. The relation is based on the moment of inertia of a cracked beam section I_{II} and the bending moment capacity M_{Rd} of a simply supported beam subjected to a static point load in the middle of the beam.

of plastic impact and an equivalent single degree of freedom system (SDOF) as described in e.g. [3, 24]. Based on the input data in Figure 12, the kinetic energy of the drop weight just prior to impact is

$$E_{\mathrm{k},0} = \frac{m_{\mathrm{w}} v_{\mathrm{y}}^2}{2} = 541 \text{ Nm} \tag{4}$$

Assuming plastic impact, the external work acting on the concrete beam is

$$W_{\mathrm{e}} = \frac{m_{\mathrm{w}}}{m_{\mathrm{w}} + m_{\mathrm{b}}} E_{\mathrm{k},0} \tag{5}$$

where $m_{\mathrm{b}} = \kappa_{\mathrm{mF}} m_{\mathrm{beam}}$ is the effective mass of the beam. For a beam with a plastic response, and subjected to a point load, it was shown that $\kappa_{\mathrm{mF}} = 0.333$ [24]. Together with $m_{\mathrm{beam}} = 24$ kg (mass of beam within span length 1 m), $m_{\mathrm{b}} = 8$ kg. From this, the external work in (5) is determined as $W_{\mathrm{e}} = 302$ Nm.

The external work W_{e} is balanced by the internal work W_{i} in the loaded structure. Using a simplified bilinear load-displacement relation as that shown in Figure 16, the internal work is

$$W_{\mathrm{i}} = \int_0^{u_{\mathrm{tot}}} R(u)\, du = W_{\mathrm{i,el}} + W_{\mathrm{i,pl}} = \frac{R_{\mathrm{Rd}} u_{\mathrm{el}}}{2} + R_{\mathrm{Rd}} u_{\mathrm{pl}} \tag{6}$$

Taking into account the influence of both upper and lower reinforcement bars in the cross section, the moment capacity was determined as $M_{\mathrm{Rd}} = 2.84$ kNm. Assuming a cracked stiffness (state II) along the whole beam length, the load capacity and elastic deformation were determined as $R_{\mathrm{Rd}} = 11.3$ kN and $u_{\mathrm{el}} = 4.7$ mm, respectively. From (6), the plastic deformation is $u_{\mathrm{pl}} = 24.3$ mm. Therefore, the total displacement is $u_{\mathrm{tot}} = u_{\mathrm{el}} + u_{\mathrm{pl}} = 29$ mm. Comparing this displacement with $u_{\mathrm{FEM}} = 26$ mm the finite element analysis, indicates further that the numerical results are realistic for this test-setup.

5   Conclusions

Two approaches to the numerical modelling of bond, called merged and coincident with slip, for the failure analysis of reinforced concrete were investigated by means of a mesh sensitivity study and two comparisons with experiments.

The mesh sensitivity study in section 3 shows that the merged approach produces mesh dependent crack numbers and spacings. The finer the mesh is, the more cracks and therefore smaller spacings are produced. On the other hand, the coincident with slip approach produces mesh independent crack patterns, if fine enough meshes are used. Both approaches reproduce almost mesh independent load-displacement results.

The analyses of the tension stiffening experiments with plain and fibre reinforced concrete in section 4.1 show that both the merged and the coincident with slip approach are capable of reproducing smaller crack spacings for fibre reinforced concrete than for plain concrete, which is in agreement with the experimental results. However, both approaches are underestimating the number of cracks reported in the experiments. Both approaches are also capable of reproducing reasonably well the response of the drop weight impact test.

Acknowledgements

References

[1] Bažant, Z. P. and Jirásek, M. Nonlocal integral formulations of plasticity and damage: Survey of progress. *Journal of Engineering Mechanics, ASCE*, 128(10):1119–1149, 2002.

[2] Bažant, Z. P. and Oh, B.-H. Crack band theory for fracture of concrete. *Materials and Structures*, 16:155–177, 1983.

[3] Biggs, J. M. *Introduction to structural dynamics*. McGraw-Hill College, 1964.

[4] Bischoff, P. H. Effects of shrinkage on tension stiffening and cracking in reinforced concrete. *Canadian Journal of Civil Engineering*, 28(3):363–374, 2001.

[5] Bischoff, P. H. Tension stiffening and cracking of steel fiber-reinforced concrete. *Journal of materials in civil engineering*, 15(2):174–182, 2003.

[6] Casanova, A.; Jason, L., and Davenne, L. Bond slip model for the simulation of reinforced concrete structures. *Engineering Structures*, 39:66–78, 2012.

[7] CEB-FIP12. *CEB-FIP Model Code 2010, Design Code*, 2012.

[8] CEB-FIP91. *CEB-FIP Model Code 1990, Design Code*. London, 1991.

[9] Červenka, J. and Papanikolaou, V. K. Three dimensional combined fracture-plastic material model for concrete. *International Journal of Plasticity*, 24(12):2192–2220, 2008.

[10] Červenka, V.; Jendele, L., and Červenka, J. ATENA program documentation, Part 1: Theory. *Praha, Czech Republic*, 2005.

[11] DIANA, TNO. DIsplacement method ANAlyser. *Users Manual, Release*, 9(3), 2015.

[12] Gomes, H. M. and Awruch, A. M. Some aspects on three-dimensional numerical modelling of reinforced concrete structures using the finite element method. *Advances in Engineering Software*, 32(4):257–277, 2001.

[13] Grassl, P. Quasi-static three point bending lS-Dyna analyses with MAT CDPM (MAT 273) using tetra-and hexahedral meshes. Research report, School of Engineering, University of Glasgow, 2016.

[14] Grassl, P. and Jirásek, M. Damage-plastic model for concrete failure. *International Journal of Solids and Structures*, 43:7166–7196, 2006.

[15] Grassl, P.; Xenos, D.; Nyström, U.; Rempling, R., and Gylltoft, K. CDPM2: A damage-plasticity approach to modelling the failure of concrete. *International Journal of Solids and Structures*, 50(24):3805–3816, 2013.

[16] Hallquist, J. O. LS-DYNA theory manual. *Livermore Software Technology Corporation*, r:8241, 2017.

[17] Hallquist, J. O. LS-DYNA keyword users manual. *Livermore Software Technology Corporation*, r:8241, 2017.

[18] Jansson, A.; Flansbjer, M.; Löfgren, I.; Lundgren, K., and Gylltoft, K. Experimental investigation of surface crack initiation, propagation and tension stiffening in self-compacting steel–fibre-reinforced concrete. *Materials and Structures*, 45(8):1127–1143, 2012.

[19] Jason, L.; Huerta, A.; Pijaudier-Cabot, G., and Ghavamian, S. An elastic plastic damage formulation for concrete: Application to elementary tests and comparison with an isotropic damage model. *Computer Methods in Applied Mechanics and Engineering*, 195(52):7077–7092, 2006.

[20] Jendele, L. and Červenka, J. Finite element modelling of reinforcement with bond. *Computers & structures*, 84 (28):1780–1791, 2006.

[21] Jirásek, M. and Bauer, M. Numerical aspects of the crack band approach. *Computers and Structures*, 110–111: 60–78, 2012.

[22] Jirásek, M. and Bažant, Z. P. *Inelastic Analysis of Structures.* John Wiley and Sons, Chichester, 2002.

[23] Jirásek, M. and Grassl, P. Evaluation of directional mesh bias in concrete fracture simulations using continuum damage models. *Engineering Fracture Mechanics*, 75(8):1921–1943, 2008.

[24] Johansson, M. and Laine, L. Bebyggelsens motståndsförmåga mot extrem dynamisk belastning, Del 3: Kapacitet hos byggnader (Housing settlement capacity against extreme dynamic loading, Part 3: Building capacity. In swedish). Publication msb 0142-10, Swedish Civil Contingencies Agency, Karlstad, Sweden, 2000.

[25] Ju, J. W. On energy-based coupled elastoplastic damage theories: Constitutive modeling and computational aspects. *International Journal of Solids and Structures*, 25(7):803–833, 1989.

[26] Leppänen, J.; Johansson, M.; Grassl, P., and Ekström, J. Experimental and numerical investigation of drop weight impact tests on reinforced concrete and reinforced fibre beams. *International Journal of Impact Engineering*, 2017. In preparation.

[27] Lockhart, E. Modelling the failure of reinforced concrete subjected to dynamic loading using CDPM2 in LS-DYNA. Meng individual project report, University of Glasgow, 2017.

[28] Lovén, J. and Svavarsdóttir, E. L. Concrete beams subjected to drop weight impacts: Comparison of experimental data and numerical modelling. Msc thesis, Chalmers University of Technology, 2016.

[29] Menétrey, Ph. and Willam, K. J. A triaxial failure criterion for concrete and its generalization. *ACI Structural Journal*, 92:311–318, 1995.

[30] Mueller, H. S. and Haist, M. FIB, structural concrete. textbook on behaviour, design and performanceupdated knowledge of the CEB-FIP Model Code 1990. *FIB Bulletin*, 1:35–95, 2009.

[31] Nesset, J. and Skoglund, S. Reinforced concrete subjected to restraint forces. analytical and non-linear finite element analysis. Msc thesis, Chalmers University of Technology, 2007.

[32] Ngo, D. and Scordelis, A. C. Finite element analysis of reinforced concrete beams. *ACI Journal, Proceedings*, 64: 152–163, 1967.

[33] Omondi, B.; Aggelis, D. G.; Sol, H., and Sitters, C. Improved crack monitoring in structural concrete by combined acoustic emission and digital image correlation techniques. *Structural Health Monitoring*, 15(3):359–378, 2016.

[34] Pamin, J. and de Borst, R. Simulation of crack spacing using a reinforced concrete model with an internal length parameter. *Archive of Applied Mechanics*, 68(9):613–625, 1998.

[35] Peerlings, R. H. J.; de Borst, R.; Brekelmans, W. A. M., and de Vree, J. H. P. Gradient-enhanced damage for quasi-brittle materials. *International Journal for Numerical Methods in Engineering*, 39:3391–3403, 1996.

[36] Phillips, D. V. and Zienkiewicz, O. C. Finite element non-linear analysis of concrete structures. In *Institution of Civil Engineers, Proceedings*, volume 61, 1976.

[37] Pietruszczak, S. T. and Mróz, Z. Finite element analysis of deformation of strain-softening materials. *International Journal for Numerical Methods in Engineering*, 17(3):327–334, 1981.

[38] Pijaudier-Cabot, G. and Bažant, Z. P. Nonlocal damage theory. *Journal of Engineering Mechanics, ASCE*, 113: 1512–1533, 1987.

[39] Reu, P. L. and Miller, T. J. The application of high-speed digital image correlation. *The Journal of Strain Analysis for Engineering Design*, 43(8):673–688, 2008.

[40] Rots, J. G. *Computational modeling of concrete fracture*. PhD thesis, Delft University of Technology, Delft, The Netherlands, 1988.

[41] Rypl, D. *Sequential and Parallel Generation of Unstructured 3D Meshes*. PhD thesis, Czech Technical University, Prague, Czech Republic, 1998.

[42] Schwer, L. Modeling rebar: The forgotten sister in reinforced concrete modelling. In *13th International LS-DYNA Conference*, pages 1–28. Dynamore, 2014.

[43] Schwer, L. Modeling pre and post tensioned concrete. In *14th International LS-DYNA User Conference*, pages 1–22. Dynamore, 2016.

[44] Shi, Y.; Li, Z.-X., and Hao, H. Bond slip modelling and its effect on numerical analysis of blast-induced responses of rc columns. *Structural Engineering and Mechanics*, 32(2):251–267, 2009.

[45] Sluys, L. J. and de Borst, R. Failure in plain and reinforced concretean analysis of crack width and crack spacing. *International Journal of Solids and Structures*, 33(20-22):3257–3276, 1996.

[46] Xenos, D. and Grassl, P. Modelling the failure of reinforced concrete with nonlocal and crack band approaches using the damage-plasticity model CDPM2. *Finite Elements in Analysis and Design*, 117:11–20, 2016.

[47] Xenos, D.; Grégoire, D.; Morel, S., and Grassl, P. Calibration of nonlocal models for tensile fracture in quasi-brittle heterogeneous materials. *Journal of the Mechanics and Physics of Solids*, 82:48–60, 2015.